Magma reservoir below Sabancaya volcano (Southern Peru) imaged by broadband magnetotellurics

J.L. Torres[123], S. Byrdina[3], Y. T. Antayhua[2], G. Romero-Beltran[3], V. Rath[4], S. Garambois[3], H. Tavera[12], M. Milla[1]

[1] Pontificia Universidad Católica del Perú, Av. Universitaria, San Miguel, Lima, Perú, jose25.torres@gmail.com, milla.ma@pucp.edu.pe

[2] Instituto Geofísico del Perú, Observatorio Vulcanológico del Sur, Asentamiento Humano José María Arguedas Zona A Mz. D Lt. 08, Sachaca, Arequipa, Perú, htavera@igp.go.pe

[3] Université Grenoble Alpes, Université Savoie Mont Blanc, CNRS, IRD, Univ. Gustave Eiffel, ISTerre, 38000 Grenoble, France, svetlana.byrdina@univ-smb.fr , Stephane.Garambois@univ-grenoble-alpes.fr

[4] Dublin Institute for Advanced Studies, 5 Merrion Square, Dublin, Ireland, vrath@cp.dias.ie

SUMMARY

The Ampato-Sabancaya volcanic complex (ASVC), the Hualca-Hualca volcano (HHV), and the neighboring fault system (Huambo-Cabanaconde) associated with the Colca canyon (southern Peru) constitute a zone of recent volcanic and tectonic activity. Here, we present a 3D electrical resistivity map inverted from MT measurements acquired using broadband Metronix instruments on 33 sites in November 2022. We compare the resistivity map to results from seismological and geodetic studies. We also discuss the current conceptual model of magma supply in the area. The resistivity map exhibits high contrast resistivity regions and several extended conductive bodies. We analyze these structures based on their depths and lateral locations relative to the volcanic edifices and fault systems. Below the shallow hydrothermal system, two interconnected conductors (<0.5 Ωm) are imaged: between ~12.5 and 18 km and between ~2 and 8 km below the surface, in areas characterized by long-term deformation and intense seismicity. We interpret both conductors as a magmatic reservoir feeding the Hualca-Hualca and Ampato-Sabancaya volcanoes. Above the western branch of this reservoir, in the Huambo-Cabanaconde fault zone, a highly conductive body (<0.2 Ωm) is imaged between 2 and 7 km below the surface. Because of the extremely low resistivity of this body, we interpret it as ultra-saline brines originating from the magmatic reservoir and emplaced (or replenished) during the unrest episode in 2013. Another conductor is found East of the Ampato volcano in an aseismic area with no surface hydrothermal manifestations. We associate this body with a fossil hydrothermal system remaining from past eruptions. In our interpretation, the injection of magmatic fluids from the deep magmatic chamber to the superficial zone caused the deformation observed in the volcanic area since 2013. This also caused the reactivation of the fault systems and the subsequent occurrence of intense seismic activity in the Colca Valley.

Keywords: Magnetotellurics (MT), Magmatic chamber, Sabancaya Volcano

1. INTRODUCTION

Sabancaya volcano is a stratovolcano (15° 49.3'S; 71° 52.7'W; 5960 m a.s.l.) that is part of the Central Volcanic Zone (CVZ) of the Andes and is located 75 km NW of Arequipa, the second most populated city of Peru (Fig. 2C). It is one of the most active volcanoes in the Central Andes (Pritchard et al., 2018) and has a long eruptive history since its formation to its current state.

Petrological, geodetic, and geophysical studies suggest the presence of a main magmatic chamber located ~13 km deep beneath the Hualca-Hualca volcano (Boixart et al., 2020; MacQueen et al., 2020; Machacca et al., 2023). In addition, this deep magmatic chamber would feed and interact with a shallow one (~6 km deep) located beneath the Sabancaya volcano (Gerbe and Thouret 2004). However, these studies do not provide the geometry of the chambers or the geometry of the conduits through which the magma rises, making it difficult to understand the origin of the seismicity pattern and the relationship between tectonic and volcanic activity. For this reason, it is necessary to complement the current information with other geophysical techniques. We present a 3D resistivity image of the magmatic reservoir showing the associated hydrothermal alteration zones from magnetotelluric measurements.

2. METHODS

The magnetotelluric (MT) method consists of measuring the temporal variations of the electric and magnetic field simultaneously to characterize the distribution of the electrical resistivity of the Earth's crust (Rikitake, 1948; Tikhonov, 1950; Simpson and Bahr, 2005; Chave and Jones, 2012). Under certain conditions, the method can quantify the fraction of melt in the magma body (Gaillard et al., 2003; Heise et al., 2016; Cordell et al., 2022; Jenkins et al., 2023).

In the frequency domain, for each frequency, linear relationships between the field components exist (1):

$$\begin{pmatrix} E_x \\ E_y \\ H_z \end{pmatrix} = \begin{pmatrix} Z_{xx} & Z_{xy} \\ Z_{yx} & Z_{yy} \\ T_x & T_y \end{pmatrix} \begin{pmatrix} H_x \\ H_y \end{pmatrix} \qquad (1)$$

Each element of the complex impedance tensor $\boldsymbol{Z}$ can be decomposed as an apparent resistivity (ρ_a) and a phase (φ). The third line defines the Tipper, often visualized as induction arrows (see Figure 1). Phase tensors play a crucial role in MT analysis and inversion. This quantity is defined as follows (2):

$$\boldsymbol{\Phi} = \Re(\mathbf{Z})^{-1}\Im(\mathbf{Z}). \qquad (2)$$

This phase tensor has the advantage of not being affected by galvanic distortion (Caldwell et al., 2004).

2.1 DATA

The magnetotelluric measurements were acquired between November and December 2022 using four broadband ADU-08 Metronix instruments, non-polarizable electrodes, and induction coils MFS06e, sensitive in a period range between 10^{-4} and 10^{4} s. The MT data were acquired at 33 sites around the CVAS and VHH (Fig. 1), at 3 to 7 km site-to-site distances. Tippers were measured at 15 sites. The period range of the study is 0.001 s to 5000 s. At each site, data were recorded from 30 to 40 hours.

2.2 PROCESSING AND INVERSION

The ProcMT software and the robust multivariate FFMT processing tool (Hering, 2019) were used to process the data collected in each probed site using pairs of simultaneously recorded MT soundings. Figure 1 shows examples of processing results for two stations (HLC3 and QALL): the apparent resistivity (top panel) and the phase curves (middle panel) of the main diagonal components, XY and YX, as well as the induction arrows (bottom panel). The consistency between apparent resistivity and phase was tested by the Rho+ criterion (Parker and Booker, 1996). In our case, less than 5% of the raw data were removed due to this criterion.

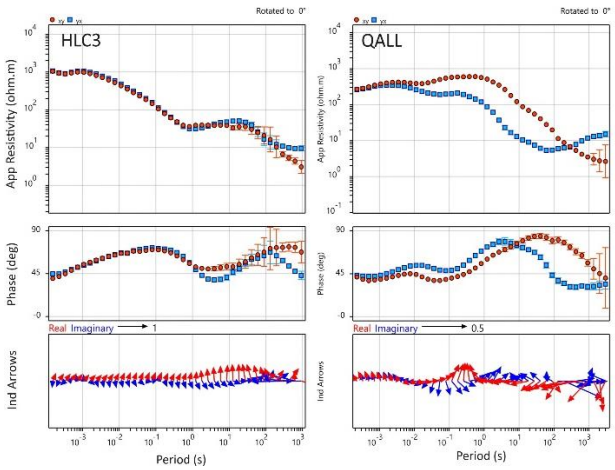

Figure 1. Apparent resistivity (top panel) and phase of the XY-YX components (middle); bottom panel corresponds to the induction arrows, as an example of data quality and processing.

2.3 3D INVERSION

The ModEM inversion code (Kelbert et al., 2014) was employed to estimate the resistivity maps. To specify the topography, an SRTM digital elevation model was used (30 m resolution), combined with less resolved bathymetry data (450 m resolution). The horizontal dimensions in the central zone were 950 m x 950 m. Because of the strong topography, the cell thickness was kept constant (50 m) for the first 3000 meters of depth. Beyond this, an increment factor of 1.1 was considered to account for the loss of resolution with depth. The total grid with 12 horizontal boundary cells counted 69x79x105 cells. Homogeneous prior models were used with 100, 50, and 30 Ωm (best misfit with 50 Ωm). We first performed impedance inversion with a high smoothing factor (α=0.5). The output model was afterward used as a starting model for phase tensor-tipper inversion (α=0.3). Static shift correction was performed at this stage, and finally, the impedance tensor was inverted again with an output of the phase tensor-tipper model as a prior model (α=0.3). Error floors accepted on Z_{xx}, Z_{yy}, Z_{xy}, and Z_{yx} were 45%, 12%, 7%, and 7% of absolute value. Fixed errors were accepted on Phase tensor components P_{xx}, P_{xy}, P_{yx}, and P_{yy} were 0.15, 0.2, 0.2, and 0.15, respectively. Fixed errors were also accepted for tippers for T_x and T_y as 0.03 and 0.05. The final model achieved an nRMS value of less than 1.1 after 33 iterations.

3 RESULTS

Figure 2 shows vertical cross-sections in N-S (Fig. 2A) and E-W directions (Fig. 2D) and a horizontal

section at 10 km below sea level (Fig. 2B). We see three conductive anomalies under ASVC and HHV. A shallow conductor (C1) below the surface is observed at ~1.0 km depth with a resistivity between 1 and 10 Ωm, typical for a shallow hydrothermal system. At intermediate depths, the conductor body C2.1 extends between ~2.0 km and 8 km beneath the Sabancaya volcano. Its resistivity goes from 1.0 to 4.0 Ωm. Beneath the Ampato volcano, conductor body C2.2 extends between ~3.0 km and 10.0 km depth with resistivities < 1.2 Ωm. This is an unexpected result since there is no evidence of thermal springs or seismic activity at the surface. Meanwhile, C2.3 represents the most conductive anomaly with 0.1 Ωm resistivity, which extends from ~2.0 km to 7.0 km depth below the Huambo-Cabanaconde zone. Finally, conduit C3 is located at ~12.5 km and extends to ~18 km depth under the Hualca-Hualca.

4 Discussion and Conclusions

We associate the C3 body with the magmatic chamber below the Hualca-Hualca volcano (~12-18 km below the surface). This is in good agreement with the deformation models of Boixart et al. (2020). Beneath the Sabancaya volcano, the C2.1 conductor could be associated with the transitional zone of magmatic fluids. Petrological studies inferred a shallow dacitic magmatic chamber at ~6 km depth (Gerbe and Thouret, 2004). In our conceptual model (following McQueen et al., 2020), the changing pressure related to the influx and transfer of magma (from C3 to C2.1) could generate seismic activity, as well as surface deformation, described by McQueen et al. (2020) and Boixart et al. (2020). This is shown in Figure 3, right panel.

Likewise, under the Huambo-Cabanaconde fault zone (E-W profile), conductor C2.3 is associated with intrusions of ultra-saline brines, reactivated in the stage of volcanic unrest of Sabancaya (from February to July 2013) subsequent surface deformation (July 2013) and fault activation, causing the occurrence of seismic swarms in July 2013 (Jay et al. 2015). The conductor (C2.2) is interpreted as an ancient hydrothermal system remaining from past eruptions.

Future work includes a sensitivity study and a quantitative interpretation of the conductors, C2.2 (“brines”) and C3 (“magma”). This will require knowledge of petrophysical parameters on magma composition and storage conditions (composition, H_2O content, temperature) and a phase equilibria model (e.g., following Cordell et al., 2022). Sensitivity studies are in progress to analyze the robustness of the resistivity values or the geometry of the bodies of interest to noise and parameters considered in the inversion. For this purpose, the fully non-linear forward model of the inverted structures will be analyzed. Jacobian-based

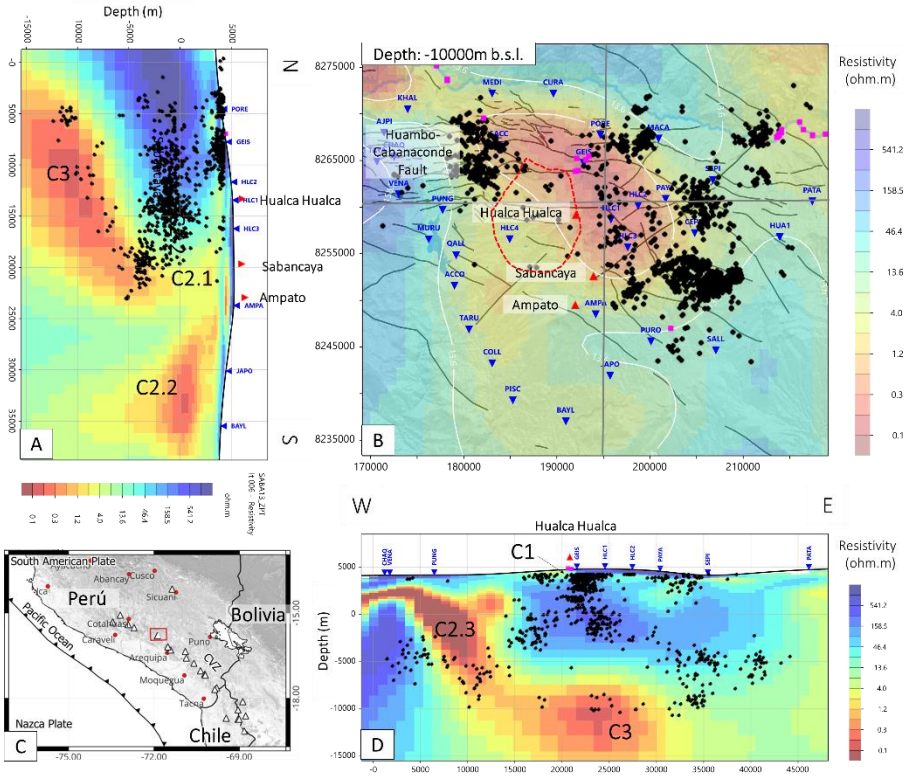

Figure 2. Vertical and horizontal resistivity profiles extracted from the 3D inversion model with seismicity from 2013 to 2020 (black circles). A) and D) show vertical sections in N-S and W-E directions. B) Horizontal section obtained at 10 km below sea level, with hypocenter of VT events (black circles) between 10 km and 15 km depth below the surface. The red dashed line marks the zone of highest inflation (20 cm) between 2015 to 2020. C) Location of study area.

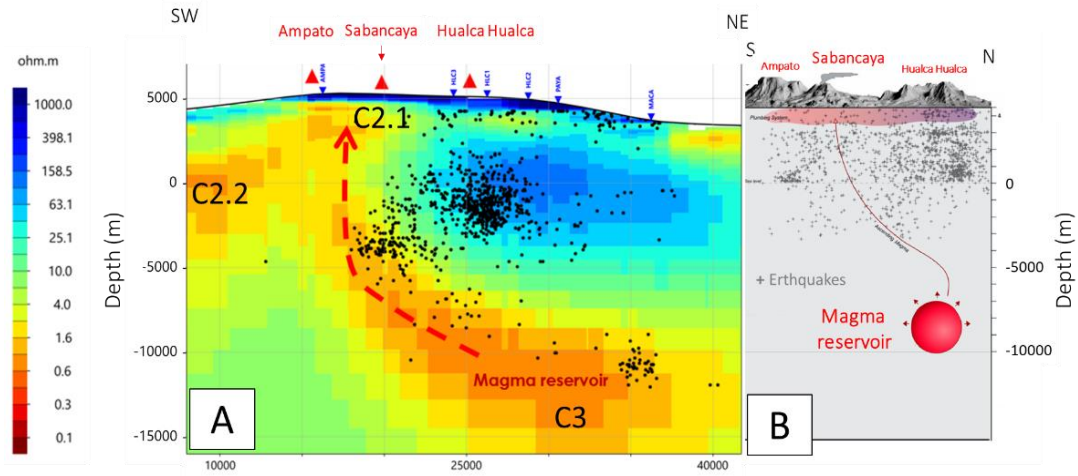

Figure 3. Conceptual resistivity model and geodetic scheme proposed by Boixart et al. (2020). The dashed red arrow are the possible upward trajectories of the magmatic fluid towards the Sabancaya conduit. The solid red circle represents the magmatic chamber interpreted by the geodetic survey. In Figure 3A, the plotted earthquakes belong to the catalog of earthquakes relocated by Machacca et al. (2023) between 2013 and 2020.

sensitivities for all inversion parameters will also be estimated.

ACKNOWLEDGMENTS

The present work is being developed within the framework of the agreement between the Instituto Geofísico del Perú (IGP) and the Institut de Recherche pour le Développement (IRD)-France. The acquisition of magnetotelluric data carried out between November and December 2022 was financed by the IRD, IGP, BQR of ISTerre, and the "Tellus Program of CNRS-INSU." All the computations presented in this paper were performed using the GRICAD infrastructure (https://gricad.univ-grenoble-alpes.fr) supported by Grenoble research communities.

REFERENCES

Boixart, G., Cruz, L. F., Miranda Cruz, R., Euillades, P. A., Euillades, L. D. & Battaglia, M. (2020). Source model for Sabancaya volcano constrained by DInSAR and GNSS surface deformation observation. Remote Sensing, 12(11), 1852.

Caldwell, T. G., Bibby, H. M., & Brown, C. (2004). The magnetotelluric phase tensor. Geophysical Journal International, 158(2), 457-469.

Chave, A. D., & Jones, A. G. (2012). The Magnetotelluric.

Hering, P. (2019). Advances in magnetotelluric data processing, interpretation and inversion, illustrated by a three-dimensional resistivity model of the Ceburoco volcano. PhD thesis, Frankfurt (Main), Univ., Diss., 2019.

Gaillard, F., Schmidt, B., Mackwell, S., & McCammon, C. (2003). Rate of hydrogen–iron redox exchange in silicate melts and glasses. Geochimica et Cosmochimica Acta, 67(13), 2427-2441.

Gerbe, M. C. & Thouret, J. C. (2004). Role of magma mixing in the petrogenesis of tephra erupted during the 1990–98 explosive activity of Nevado Sabancaya, southern Peru. Bulletin of Volcanology, 66, 541-561.

Guo, X., Li, B., Ni, H., & Mao, Z. (2017). Electrical conductivity of hydrous andesitic melts pertinent to subduction zones. Journal of Geophysical Research: Solid Earth, 122(3), 1777–1788. doi:10.1002/2016JB013524.

Jenkins, A. P., Rust, A. C., Blundy, J. & Biggs, J. (2023). Magnetotelluric investigations at Andean volcanoes: Partial melt or saline magmatic fluids? Journal of Volcanology and Geothermal Research, 440, 107852.

Machacca, R., Lesage, P., Tavera, H., Pesicek, J. D., Caudron, C., Torres, J. L., ... & Burgisser, A. (2023). The 2013–2020 seismic activity at Sabancaya Volcano (Peru): Long lasting unrest and eruption. Journal of Volcanology and Geothermal Research, 435, 107767.

MacQueen, P., Delgado, F., Reath, K., Pritchard, M. E., Bagnardi, M., ... & Miranda, R. (2020). Volcano-Tectonic Interactions at Sabancaya Volcano, Peru: Eruptions, Magmatic Inflation, Moderate Earthquakes, and Fault Creep. Journal of Geophysical Research: Solid Earth, 125(5), e2019JB019281.

Method: Theory and Practice. Cambridge University Press.

Parker, R. L. & Booker, J. R. (1996). Optimal one-dimensional inversion and bounding of magnetotelluric apparent resistivity and phase measurements. Physics of the Earth and Planetary Interiors, 98(3-4), 269-282.

Pritchard, M. E., Biggs, J., Wauthier, C., Sansosti, E., Arnold, D. W., Delgado, F., ... & Zoffoli, S. (2018). Towards coordinated regional multi-satellite InSAR volcano observations: results from the Latin America pilot project. Journal of Applied Volcanology, 7(1), 5.

Rikitake, T. (1948). Notes on electromagnetic induction within the Earth. Bull. Earthquake Res. Inst., 24:1–9.

Simpson, F. & Bahr, K. (2005). Practical Magnetotellurics, Cambridge University Press.

Tikhonov, A. (1950). On investigation of electrical characteristics of the deep layers of the Earth's crust. Dokl. Akad. Nauk SSSR, 73:295–297.

Vozoff, K. (1972). The magnetotelluric method in the exploration of sedimentary basins. Geophysics, 98-141.